Journal of Manufacturing Processes 90 (2023) 125–138

Contents lists available at ScienceDirect

Journal of Manufacturing Processes

journal homepage: www.elsevier.com/locate/manpro

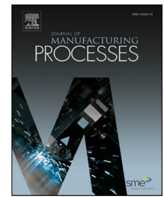

Oblique nanomachining of gallium arsenide explained using AFM experiments and MD simulations

Pengfei Fan [a], Nirmal Kumar Katiyar [b], Saurav Goel [b,c,*], Yang He [d], Yanquan Geng [d], Yongda Yan [d], Hui Mao [e], Xichun Luo [a,**]

[a] Centre for Precision Manufacturing, DMEM, University of Strathclyde, Glasgow G1 1XQ, UK
[b] London South Bank University, 103 Borough Road, London SE1 0AA, UK
[c] University of Petroleum and Energy Studies, Dehradun 248007, India
[d] Center for Precision Engineering, Harbin Institute of Technology, Harbin 150001, PR China
[e] Key Laboratory of Biomass Chemical Engineering of Ministry of Education, Zhejiang University, Hangzhou 310027, PR China

A R T I C L E I N F O

Keywords:
Plastic flow
Atomic force microscope
MD simulation
GaAs

A B S T R A C T

Gallium Arsenide (GaAs) continues to remain a material of significant importance due to being a preferred semiconductor substrate for the growth of quantum dots (QDs) and GaAs-based quantum devices used widely in fifth-generation (5G) wireless communication networks. In this paper, we explored aspects of oblique nanomachining to investigate the improvement in the machining quality as well as to understand plasticity and transport phenomena in GaAs using atomic scale machining experiments and simulations. We studied the influence of the direction vector of the cutting tip (e.g. tip alignment) during the surface generation process in GaAs. We noticed a novel observation that when the AFM tip's cutting edge presented two acute angles (i.e., 30° angles each) between the cutting face and the cutting direction (which can be regarded as an oblique cutting condition), the cutting configuration involved early avalanche of dislocations compared to other tip configurations (e.g., orthogonal cutting). Orthogonal cutting involved the least coefficient of friction but the highest specific cutting energy compared to oblique cutting. High-resolution transmission electron microscopy (HRTEM) examination revealed that the shuffle-set slip on the {1 1 1} slip system due to the ⟨1 1 0⟩ type dislocation paves the way for plasticity during nanometric cutting of GaAs. Overall, a particular condition of oblique cutting was inferred to be the best for nanofabrication of high-quality wafers using an AFM.

1. Introduction

In 2020, fifth-generation (5G) wireless technology rolled out globally and it has become a key enabling technology behind modern virtual reality (VR)/augmented reality (AR) assisted technologies [1]. 5G technology requires a multi-Gbps peak data transmission speed which is 100 times faster than 4G technology. To meet such high data transmission speeds, single crystal Gallium Arsenide (GaAs) based quantum devices have been the front runner [2]. Due to wider band gap, higher critical breakdown electric field, higher electron saturation rate and electron mobility rate than silicon, GaAs find applications in key components for power amplifiers [3], radio frequency (RF) switches [4] and low noise amplifiers [5–7].

However, the growth of quantum dots (QDs) on GaAs-based quantum devices is extremely fastidious due to the poor surface finish of the GaAs substrates [8,9]. Cutting of GaAs by mechanical means involves several competing mechanisms including ductile fracture, brittle fracture, dislocation mobility and mass transport in the stressed regions.

Chemo-mechanical polishing (CMP) [10,11] and lapping [12,13] are popularly employed to fabricate high-quality machined surfaces. Focused ion beam (FIB) milling has also been extended to fabricate 3D hemispherical cavity on the GaAs substrate [14]. However, poor yield and the risk of ion contamination on the finished surfaces render FIB the last choice. More recently, single point diamond turning (SPDT) was used to machine GaAs substrates in ductile-mode cutting [15]. SPDT process could not achieve sub-10 nm resolution and given the fact that the feed mark left by the tool on the machined surface can cause interference patterns, the SPDT method can only be used as a secondary

* Correspondence to: S. Goel, London South Bank University, 103 Borough Road, London SE1 0AA, UK.
** Corresponding author.
E-mail addresses: GoeLs@Lsbu.ac.uk (S. Goel), xichun.luo@strath.ac.uk (X. Luo).

https://doi.org/10.1016/j.jmapro.2023.01.002
Received 30 June 2022; Received in revised form 18 November 2022; Accepted 2 January 2023
Available online 11 February 2023
1526-6125/© 2023 The Author(s). Published by Elsevier Ltd on behalf of The Society of Manufacturing Engineers. This is an open access article under the CC BY license (http://creativecommons.org/licenses/by/4.0/).

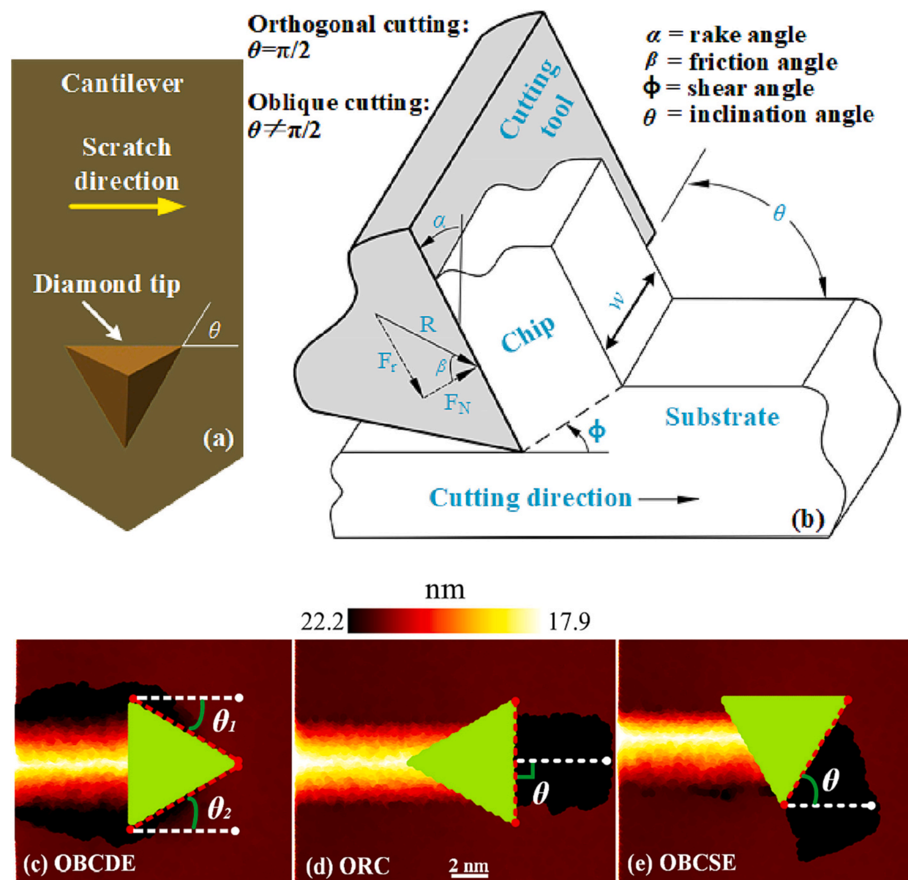

Fig. 1. Schematic of AFM-based nanometric cutting (a and b). Snapshots of MD simulation of cutting configurations (c) Oblique cutting with double edges (OBCDE) (d) Orthogonal cutting (ORC) and (e) Oblique cutting with single edge (OBCSE).

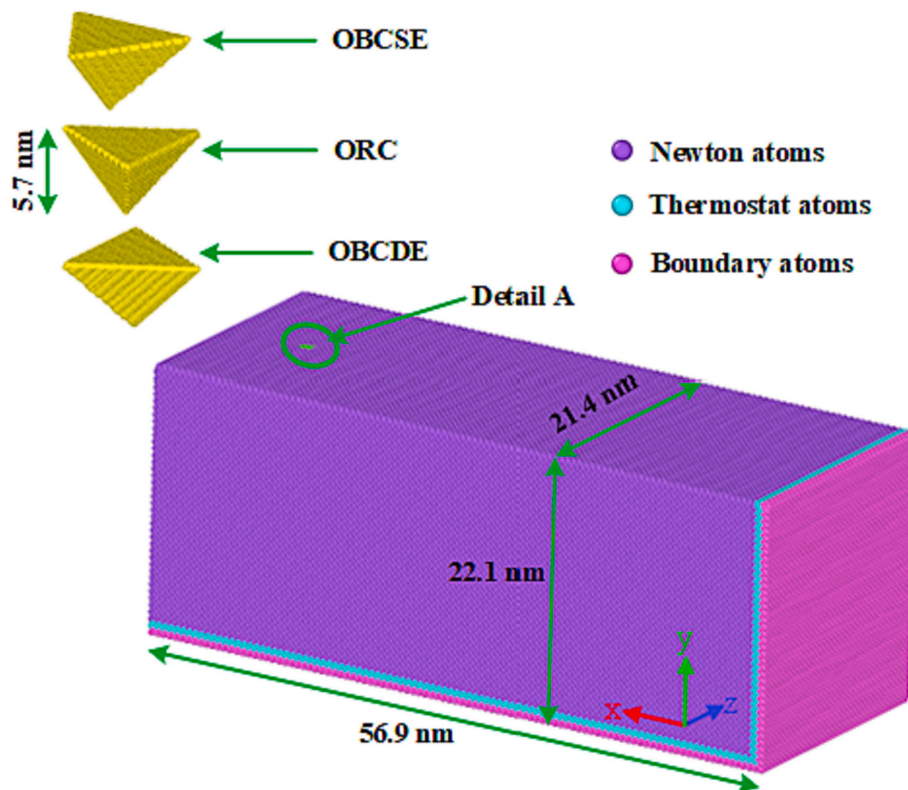

Fig. 2. Nanometric cutting model of single crystal GaAs. Detail A identifies region of atoms used to estimate the cutting stresses based on individual stress tensor acting on each atom during the cutting process.

Table 1
Simulation parameters used for the MD simulations.

GaAs substrate dimensions	56.9 nm × 22.1 nm × 21.4 nm (X, Y and Z directions)
Number of atoms in the GaAs substrate	1,188,564
Cutting tool material	Diamond tool which was assumed as a rigid body
Number of carbon atoms in the tip	17,132
GaAs lattice constant	5.65 Å (zinc blende lattice structure)
Diamond lattice constant	3.56 Å (diamond cubic lattice structure)
Depth of cut	3 nm
Cutting velocity used in MD	10 m/s
Machining distance prescribed in MD	10 nm
Machining time simulated in MD	1 ns
Crystallographic plane of the GaAs	(0 0 1)
Cutting direction	⟨1 1 0⟩
Equilibration temperature	300 K
Timestep of MD calculation	1 fs

manufacturing protocol when it concerns electronic device fabrication.

Since the invention of scanning probe microscopy (SPM) [16], the scanning probe lithography (SPL) approach [17,18] has been widely applied for the production of superior quality nanostructures [19]. A mix-and-match lithography approach where SPL is combined with etching techniques can produce a potential hybrid technology that can meet the demand for mass production shortly [20,21]. As discussed in the recent review [22], SPL technology is poised to make a significant impact on our general lives due to it being a key enabling technology in various sectors. For instance, SPL would continue to be used in applications such as (i) nanocircuitry fabrication and diagnosis of package-on-package and system-in-package products (ii) Quantum computing, and data storage devices to fabricate quantum dots (iii) biomedical applications to engineer the surface of tissue scaffold to manipulate cell response (iv) nanofluidic devices for physical confinement to study the response of single molecules and drug design and so on.

During SPL, a prismatic shape tip (made of diamond) performs the role of a cutting tool akin to micromachining. An unavoidable problem during this process is that the alignment of the prism shaped diamond tip can significantly influence the quality of machining. Since GaAs is hard and brittle [23], the mechanics of oblique and orthogonal nanomachining is worth investigating to find out the differences in the quality of machining. Accordingly, this work made use of AFM experiments and MD simulations to comprehensively examine the differences in oblique and orthogonal nanomachining of single crystal GaAs as our continued efforts in this direction [24–26]. In the past, Hyon et al. [27] employed a diamond tip to generate 10 nm nanogrooves on the GaAs surface. However, this work only proved that SPL is practically useable for prototyping GaAs-based nanostructures and nanodevices. The issue of tip alignment was not investigated. We addressed this issue using a combined simulation and experimental approach. For the simulation, we used molecular dynamics (MD) as a reliable atomic-scale approach [28–30]. On the experimental front, we used AFM scratching followed by post-processing using transmission electron microscopy (TEM). With this approach, we report novel insights into the mechanical behaviour of GaAs while subjecting to contact loading AFM cutting under orthogonal and oblique conditions. Through this paper, we report how the tip alignment influences the plastic flow and the coefficient of friction and the specific cutting energy of GaAs.

2. MD simulation and experimental details

2.1. MD simulation methodology

A schematic diagram of the AFM-based cutting configuration is shown in Fig. 1(a) and (b), respectively. The prismatic shape tip face tilted with an inclination angle (θ) to the cutting direction presents a condition which is classed as oblique cutting. When (θ) is 90°, the cutting condition is referred to as the orthogonal cutting condition. When $\theta_1 = \theta_2 = 30°$ (see Fig. 1(c)), the "V" shaped face presents a unique condition of oblique cutting with double edges which is herein referred to as OBCDE. When $\theta = 60°$ (see Fig. 1(e)), the oblique cutting only engages a single edge of the tip which is referred to as OBCSE. When the

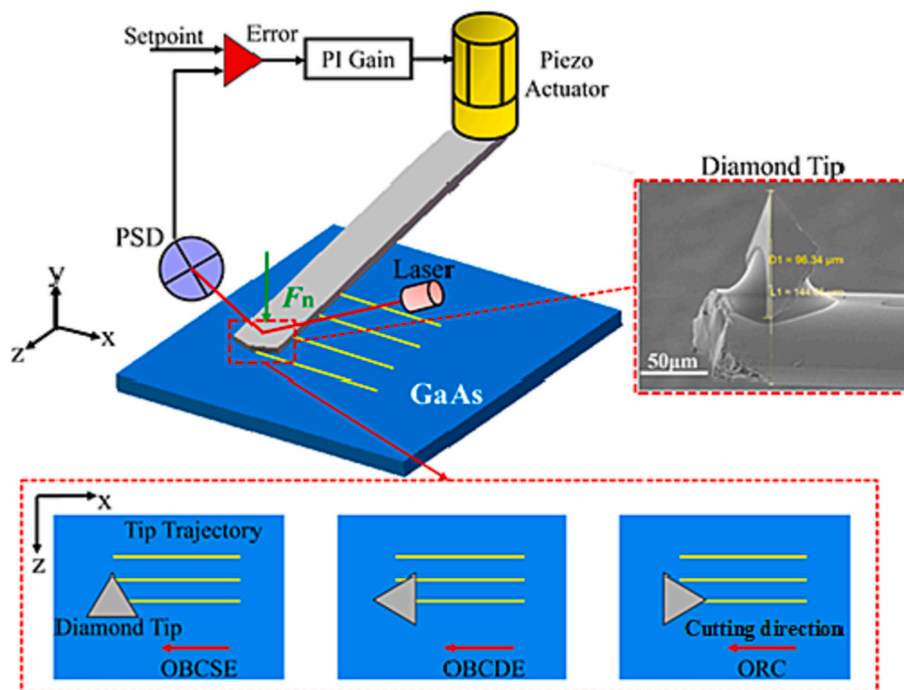

Fig. 3. The schematic of the nanomachining experiments performed on an AFM.
(Reproduced and modified with permission from reference [31]. Copyright © 2021, Springer Nature.)

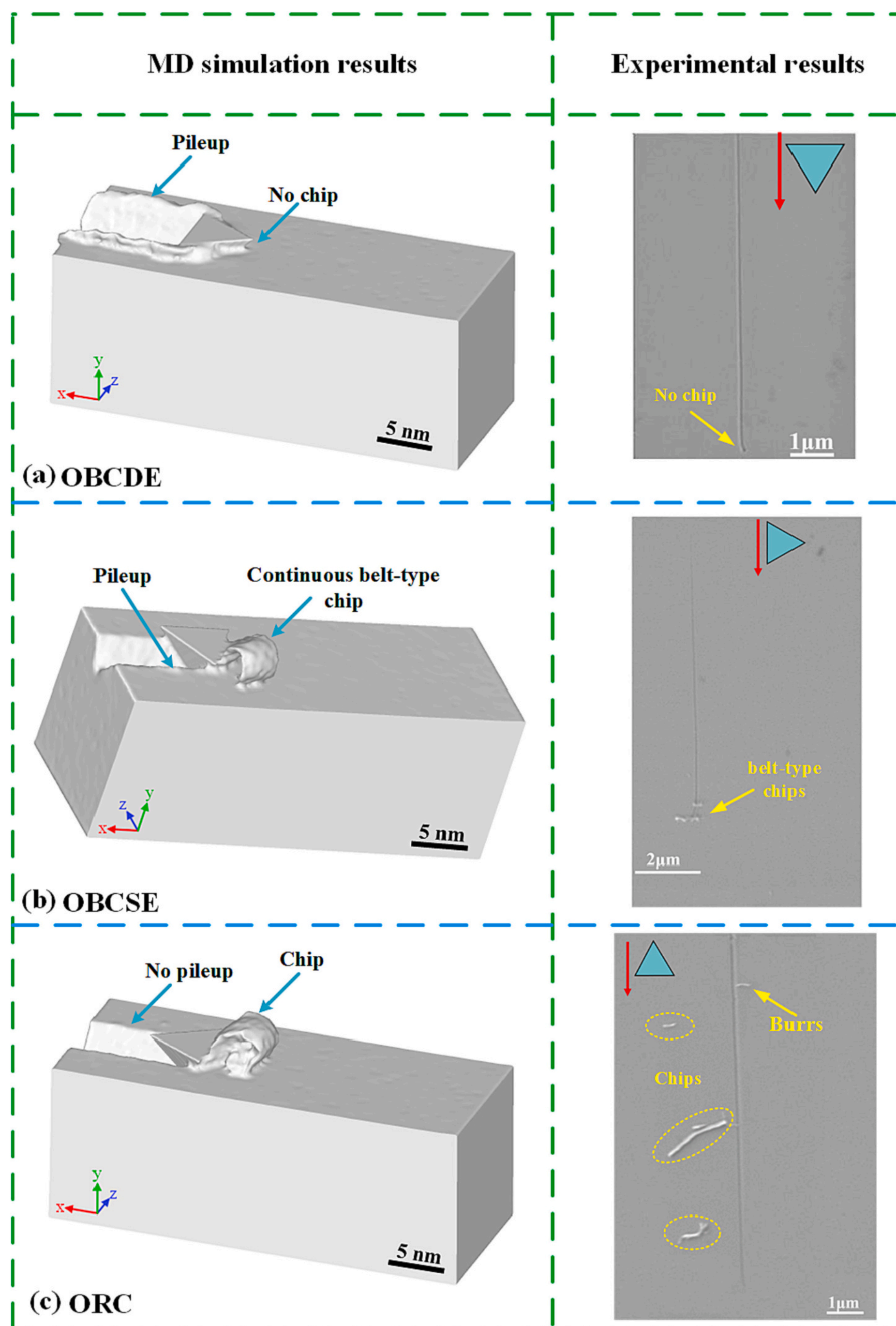

Fig. 4. Topography of cut surfaces under three configurations namely (a) OBCDE, (b) OBCSE and (c) ORC obtained from MD and AFM.

cutting face is perpendicular to the cutting direction i.e. $\theta = 90^{\circ}$ (see Fig. 1(d)), this presents an orthogonal cutting (ORC) condition. Hence, the three representative conditions investigated in this paper using MD simulations and AFM experiments were (i) oblique cutting with double edges (OBCDE), (ii) orthogonal cutting (ORC) and (iii) oblique cutting with a single edge (OBCSE), as shown in Figs. 1 and 2.

In the MD simulation model, the GaAs substrate was divided into Newton atoms, thermostat atoms and boundary atoms. Further details about the model development can be seen elsewhere [31–33]. The MD model was equilibrated for about 60 ps through a fast and robust Nose-Hoover method using an open source code "Large-scale atomic/molecular massively parallel simulator" (LAMMPS) [34]. The datasets were analysed and visualised using the Open Visualization Tool (OVITO) [35]. The model development parameters used for building the MD model are shown in Table 1.

The choice of a force field or a potential energy function can play a significant role in influencing the accuracy of MD results. We employed a hybrid scheme to describe the interactions between the Ga-Ga, As-As and C-C atoms constituting the workpiece and the diamond cutting tool. A three-body analytical bond order potential (ABOP) [36] fully parameterized for describing Ga and As atoms were used to describe the GaAs workpiece. The C—C interactions were described using the ABOP scheme [37]. The cross-interactions of Ga-C and As-C atoms were described using the Ziegler-Biersack-Littmark (ZBL) potential function

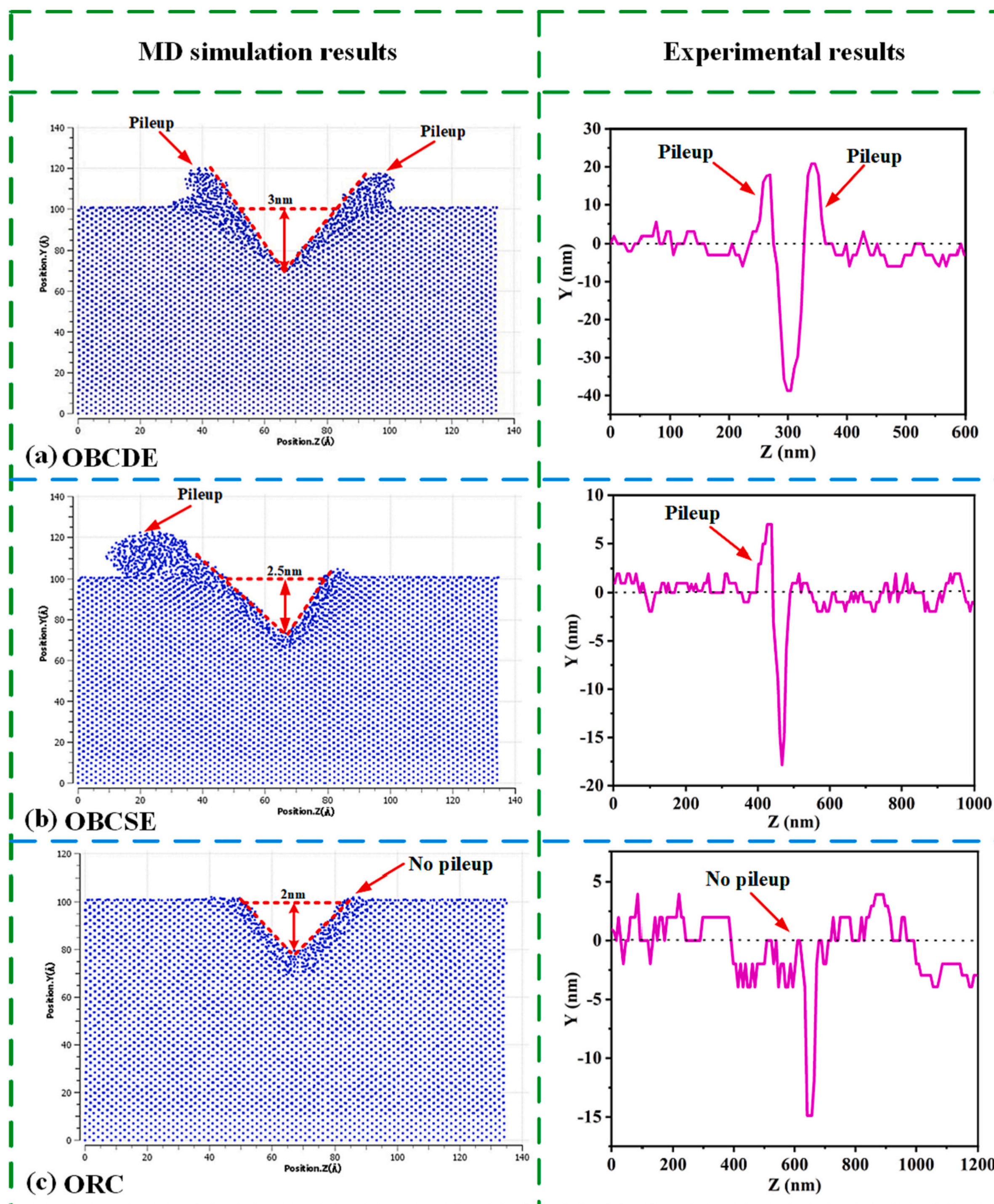

Fig. 5. Cross section view and comparison of pile up during (a) OBCDE (b) OBCSE and (c) ORC obtained from MD (velocity controlled) and AFM (force controlled) scratch tests.

[38]. The repulsive and bond integral terms were computed by Goodwin-Skinner-Pettifor (GSP) function [39]. The simulations were performed on ARCHER2 High-Performance Computer (HPC) using 12,800 cores (each node on ARCHER2 has about 128 cores) and each scratch simulation typically took about 5 h to finish.

2.2. AFM experimental setup

A generic prismatic shaped diamond tip (Micro Star Technologies Ltd., USA) with a sub 5 nm radius was used to carry out the nanometric cutting experiments on a single crystal gallium arsenide (GaAs) (0 0 1) substrate (Ø10 mm, the thickness of 0.5 mm, PI-KEM Ltd., UK) along the ⟨1 1 0⟩ direction on a commercial AFM platform with Nanoman module (Dimension Icon, Bruker Corporation, Germany).

This work made use of a customized diamond tip with a high stiffness of cantilever (200 N/m) to carry out the cutting experiments. The high stiffness of the cantilever avoided torsion (when the cutting direction is perpendicular to the cantilever) and bending (when the cutting direction is parallel to the cantilever) effects. A schematic diagram of the AFM experimental setup showing three cutting conditions namely, OBCSE,

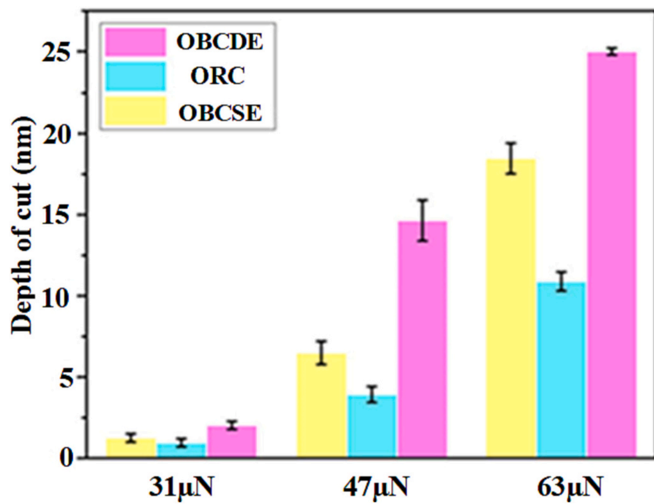

Fig. 6. Experimental result showing depth of cut achieved under different normal loads.

OBCDE and ORC is shown in Fig. 3. The diamond tip was prescribed a total scratch distance of 10 μm at a velocity of 3 μm/s for each condition with an applied voltage of 0.25 V–0.5 V. The preset normal load (F_N) was calculated as:

$$F_N = \text{voltage} \times K_N \times \text{sensitivity} \quad (1)$$

where K_N refers to the spring constant of the cantilever of the diamond tip which was 200 N/m. The sensitivity of the diamond tip after pressing it onto a sapphire specimen surface was estimated to be about 627.5 nm/V. Therefore, the normal load (F_N) range was from 31 μN–63 μN under 0.25 V–0.5 V applied voltage i.e., AFM experiments involving load control tests with three load ranges, 31 μN, 47 μN and 63 μN were performed to verify the consistency in the experimental observations.

After the experiments, a sharp silicon tip was employed to measure the morphology of nanogrooves. The scratched surface was also inspected using a scanning electron microscope (SEM) (Quanta 200FEG, FEI, USA). Furthermore, a TEM specimen (a thickness of <100 nm) of the machined area was prepared by focussed ion beam (FIB) system (Fei Helios Nanolab G3 UC DualBeam microscope) to investigate sub-surface deformation events.

3. Results and discussions

3.1. Comparison of chip morphology

Figs. 4 and 5 show a comparison of chip morphology observed through the experiments compared against MD simulations in each case. Under the OBCDE cutting condition, the pileup on both sides of the nanogroove was observed (see Fig. 4(a)). In particular, no chips were observed on the two cutting edges. The cross-sectional profile from the AFM image demonstrated that the material got piled up evenly on both sides of the nanogroove, which corroborated with the MD simulations (see Fig. 5(a)).

This cutting condition of OBCDE is pretty unique since a sharp line contact acts as the primary rake face of the tool. Under this condition, the cutting chips of the cut material do not flow on the tool rake face conventionally, and instead, the material is simply displaced and dumped sideways. This cutting condition leads to maximum pile up and side flow of the material. This is also the reason why no chips can be seen in the SEM image (see Fig. 4(a)).

During OBCSE, a sidewall pileup and continuous belt-type chips were observed on the nanogroove surfaces in both MD simulations and experiments (see Fig. 4(b)). During ORC, it can be seen that the chip flows primarily on the leading front cutting edge ahead of the tool as shown in Fig. 4(c). The SEM observations also revealed evidence of abrupt chip breaking during ORC which indicated that when the volume of material removal reaches a certain threshold, it is dumped sideways by the tip. Also, this led to burr formation only during ORC but not for the OBCDE and OBCSE configurations, which indicates that oblique cutting can provide superior quality of machined surface than orthogonal cutting.

Further comparison of the scratched nanogroove configuration is shown in Fig. 6 (which is dependent on the applied load), under the same applied load and it consistently showed that the OBCDE condition achieved better effective cutting depth while the ORC condition lead to the least effective cutting depth. The variation in the depth of cut (DoC) and a representative lateral force while performing AFM scratching using a normal load of 47 μN is shown in Fig. 6. These results showed that the OBCDE condition created the deepest effective depth of cut (DoC) than the other two cases under all loading scenarios tested in this work. The AFM cutting forces (lateral force) showed that the magnitude of OBCDE > OBCSE > ORC, meaning more deeper cut led to an increase in the lateral force, although the normal load in all cases due to being load controlled scratching was same in all cases.

3.2. Comparison of cutting forces and specific cutting energy

A scratching operation entails two forces, scratch force (F_c in X-direction) and normal force (F_t in the Y-direction). F_s is the shear force parallel to the shear plane. F_n is the resultant force component normal to the shear plane. F is the resultant force component parallel to the tool rake face. N is the resultant force component normal to the tool rake face. Based on these forces, a schematic model to estimate the specific cutting energy during AFM-based nanomachining was developed using traditional machining theory as shown in Fig. 7.

φ and β are known as shear angle which are formed between shear plane and cutting velocity vector and the friction angle that were calculated from Eqs. (2) and (3) using Merchant's force circle [40].

$$\varphi = tan^{-1}\left(\frac{rcos\alpha}{1 - rsin\alpha}\right) \quad (2)$$

$$\beta = \frac{\pi}{2} + a - 2\varphi \quad (3)$$

where a is the rake angle.

The chip thickness ratio r can be expressed as:

$$r = \frac{t_0}{t_c} = \frac{sin\varphi}{cos(\varphi - a)} \quad (4)$$

where t_0 is the uncut chip thickness and t_c refers to cut chip thickness.

V_s is the shear velocity (chip relative to workpiece) and V_c is the chip velocity (chip relative to tip) in the velocity circle. V_s and V_c were calculated from Eqs. (5) and (6).

$$V_s = V\frac{cosa}{cos(\varphi - a)} \quad (5)$$

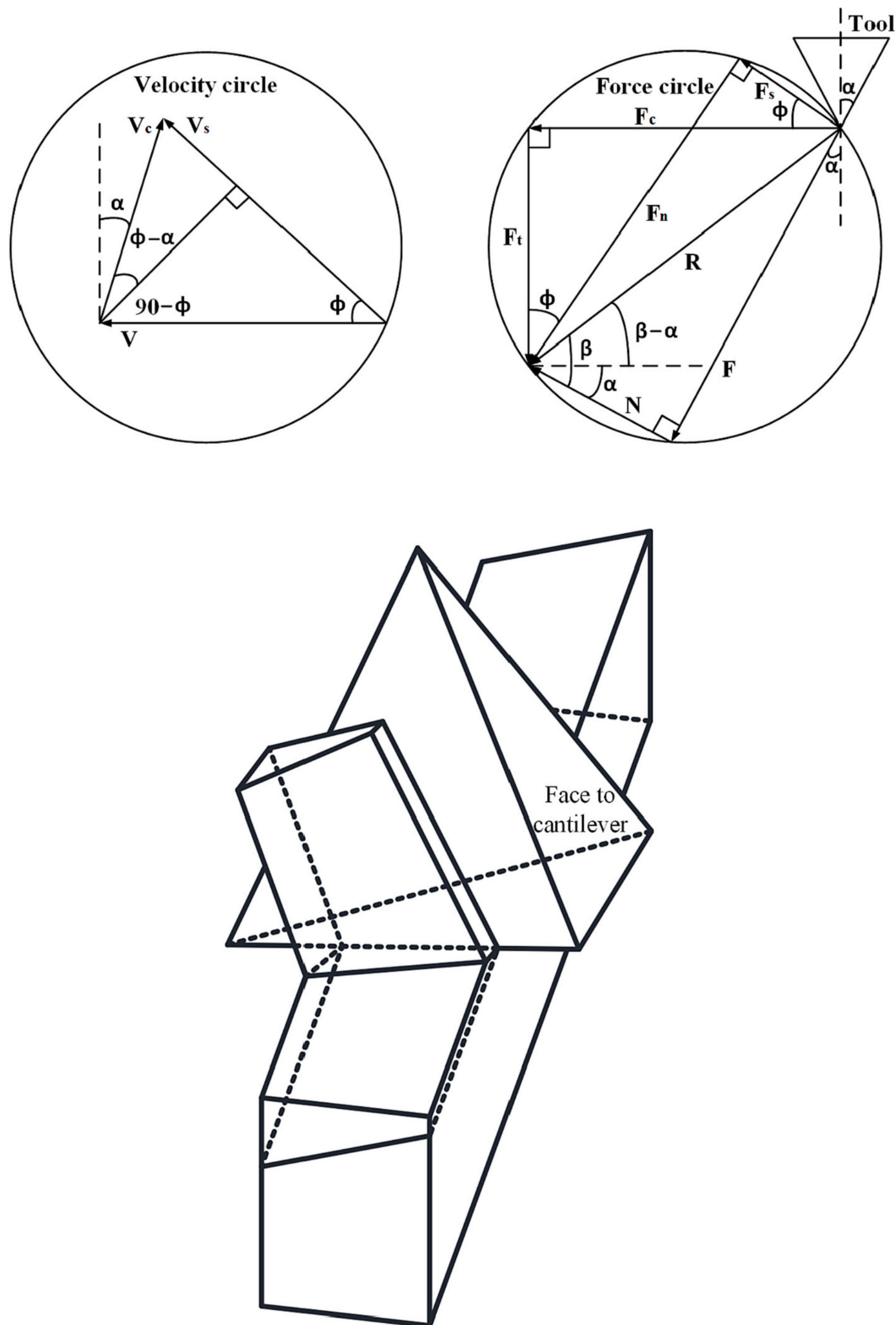

Fig. 7. Schematic diagram of chip formation during AFM-based nanomachining.

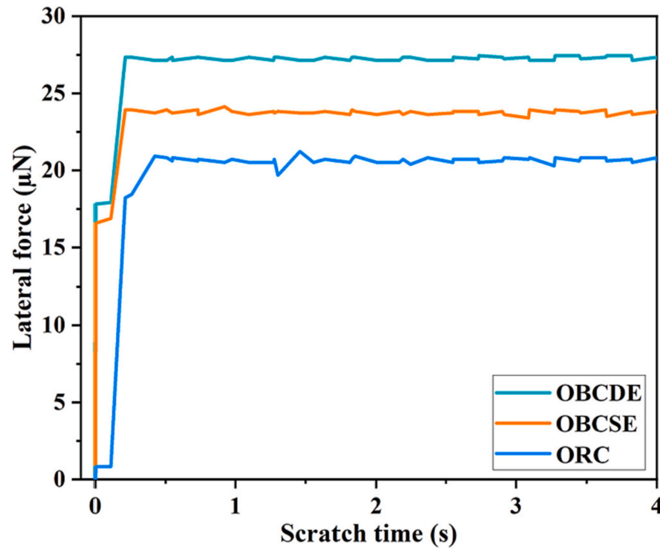

Fig. 8. Experimental results showing the variation in the lateral force at a load of 47 μN.

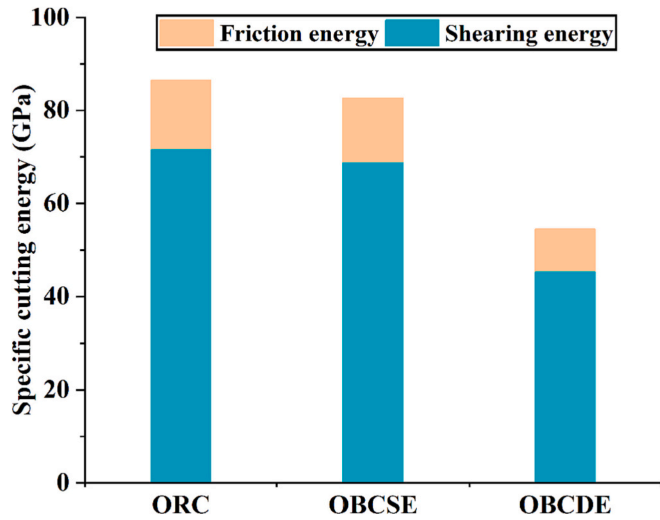

Fig. 9. Variation in friction and shear energy under three cutting configurations obtained from AFM experiments for the normal load of 47 μN.

$$V_c = V\frac{sin\varphi}{cos(\varphi - a)} \tag{6}$$

where V refers to the cutting velocity (tip relative to workpiece).

Eqs. (7)–(12) expresses different force components in terms of R, φ and β.

$$F_c = Rcos(\beta - a) \tag{7}$$

$$F_t = Rsin(\beta - a) \tag{8}$$

$$F_s = Rcos(\varphi + \beta - a) \tag{9}$$

$$F_n = Rsin(\varphi + \beta - a) \tag{10}$$

$$F = Rsin\beta \tag{11}$$

$$N = Rcos(\beta) \tag{12}$$

where R represents the resultant cutting force in the force circle (Fig. 7).

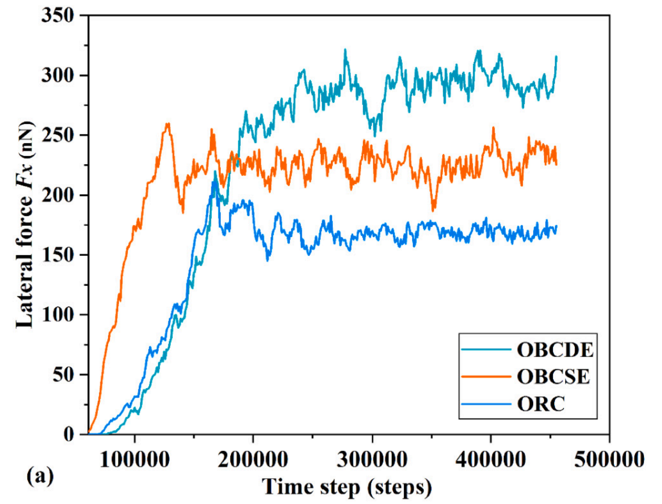

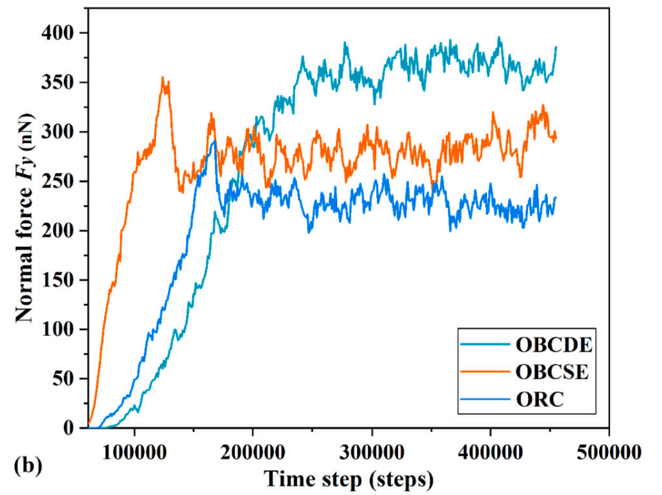

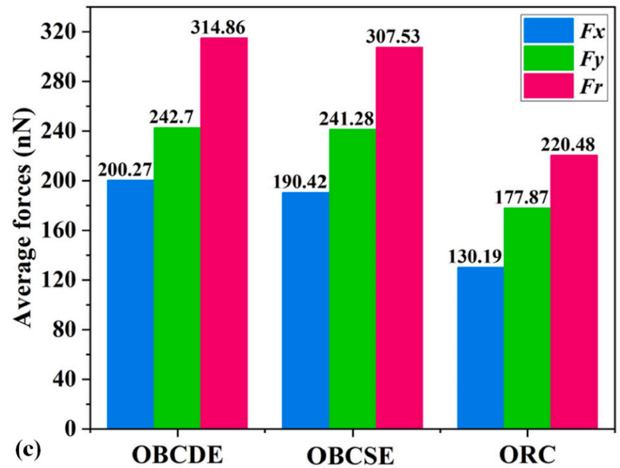

Fig. 10. The MD simulation results of variation in scratch force *Fx* (a) and *Fy* (b) with scratch distance under three cases. (c) MD simulation results for average value of lateral force *Fx*, normal force *Fy* and resultant force *Fr* for three cases.

The specific cutting energy during the nanometric cutting process is defined as the energy required for shearing the material and the energy consumed in overcoming the friction between the tool and the chip interface [41]. The specific cutting energy for shearing and friction can be expressed as Eqs. (13) and (14).

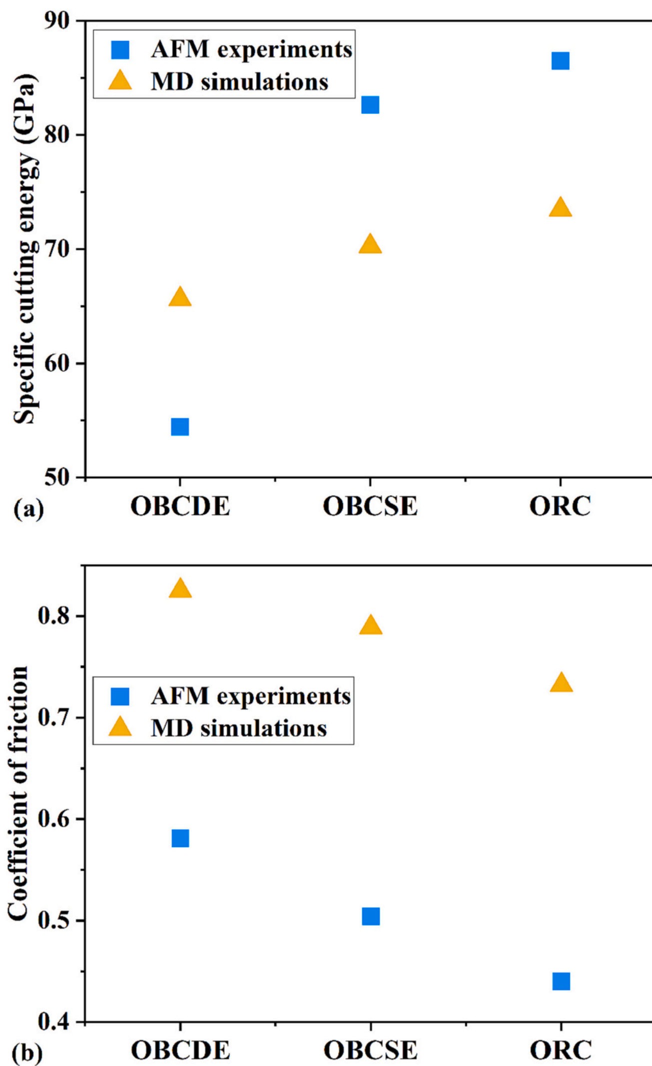

Fig. 11. Comparison of specific cutting energy and coefficient of friction obtained from the AFM experiments and MD simulations.

$$U_s = \frac{F_s V_s}{V w t_0} \tag{13}$$

$$U_f = \frac{F_t V_c}{V w t_0} \tag{14}$$

where w is out-of-plane width, which was shown earlier in Fig. 1.

Fig. 8 shows a representative cutting force (lateral force Fx) obtained from AFM experimentation when a normal force of 47 μN. The corresponding variation in the specific cutting energy revealing the partition of friction energy and shearing energy during cutting under all three configurations is shown in Fig. 9. From Fig. 9, one can see that (i) oblique cutting consumes less specific cutting energy than orthogonal cutting and (ii) OBCDE configuration showed minimal specific cutting energy and (iii) friction energy was about 17 % of the total specific cutting energy and the shearing energy was about 83 % of the total specific cutting energy. One can explain this through the analogy that the higher energy involved during orthogonal cutting is because extra energy is required to drag and displace the cutting chips ahead of the tool which is otherwise not required during OBCDE where the material is simply displaced and dumped sideways. That is why OBCDE achieved the deepest effective depth of cut in experimental results shown previously.

The cutting forces obtained from the MD simulation for all three cutting configurations tested under velocity controlled scratch process are shown in Fig. 10. In accord with the order revealed by the experiments, it can be seen that the orthogonal cutting involved the least force and achieved a lesser extent of material removal compared to the oblique cutting configurations. Moreover, the OBCSE cutting condition shows a steep rise in the force at the beginning of the cutting which suggests that a high compressive stress state sets in from the beginning of the cutting in this configuration. The same slope in the case of the other oblique cutting condition OBCDE was mild whereas that of the ORC cutting condition was intermediate.

Fig. 11 presents a comparison of the coefficient of friction and specific cutting energy obtained from the AFM experiments and the MD simulation. While the tip size in AFM and the velocity used for cutting in AFM were much larger than in the MD simulation, a good correlation in the observations can be seen. The main observations from these comparisons were (a) the specific cutting energy and coefficient of friction seem to hold an inverse relation i.e. the specific cutting energy during orthogonal cutting was largest but the coefficient of friction during orthogonal cutting was least. (b) The coefficient of friction during OBCDE was the largest and the specific cutting energy involved was the least (c) typically depending on the cutting configuration it takes about 50 to 90 GPa of specific cutting energy to cut GaAs from the AFM and the corresponding coefficient of friction (COF = Fx/Fy) during the three cutting configurations vary from 0.4 to 0.6.

It proves the initial hypothesis that the diamond tip alignment in an AFM can play a significant role in influencing the cutting conditions leading to variable outcomes including the quality of machining. In this spirit, the next section examines the propensity of defects in the GaAs wafer caused by different cutting conditions.

3.3. *Mechanism of sub-surface defects and plasticity*

Fig. 12 shows the sub-surface plastic deformation depth for (a) (b) oblique cutting and (c) orthogonal cutting while scratching the same cutting depths in the MD simulations. MD results showed that the OBCDE condition caused minimum sub-surface deformation (1.104 nm), followed by OBCSE (1.481 nm) and ORC (1.812 nm). The ratio of the depth of cut and sub-surface deformation in MD simulations was about 2.72, 2.03 and 1.66, respectively. From what was discussed previously it may be inferred that the OBCDE condition can achieve the deepest effective cutting depth for the same amount of applied load causing the least sub-surface deformation depth. That means improved sub-surface integrity can be obtained by using an OBCDE cutting configuration. This finding could raise a significant impact in fabricating high-quality GaAs-based quantum devices.

The oblique cutting mode was identified to lead to better surface integrity on the GaAs surface. Therefore, considering the wear reduction of the diamond tip, OBCSE was selected to fabricate a set of nanogrooves to directly observe the sub-surface plastic deformation. The morphology of a set of nanogrooves fabricated by OBCSE is shown in Fig. 13(a). It was observed that continuous belt-type chips could be produced by the OBCSE cutting configuration, which was consistent with the SEM observation shown earlier in Fig. 4(b). The cross-sectional sample was cut off by using a focused ion beam (FIB) perpendicular to the scratching direction and was lifted out using an in situ micromanipulator and attached to a specimen holder, as shown in Fig. 13(b)(c). The marked area in the deformation zone underneath the scratched nanogroove was analysed using the transmission electron microscope (TEM). The AFM tip affected the GaAs lattice ~65 nm deeper, as shown in Fig. 14(a) (a nanometer-scale marked). The scratch affected area was studied at different places by HRTEM, and each HRTEM image is marked with the red arrow in Fig. 14(a). The GaAs single crystal oriented in the zone axis [011] confirmed by the electron diffraction pattern is shown in Fig. 14 (b). The sidewall of the groove marked as an upper layer was seen to have an amorphous nature ~2–3 nm thickness. It showed a shallow wavy cutting, as seen in the HRTEM image Fig. 14(c) and their FFT

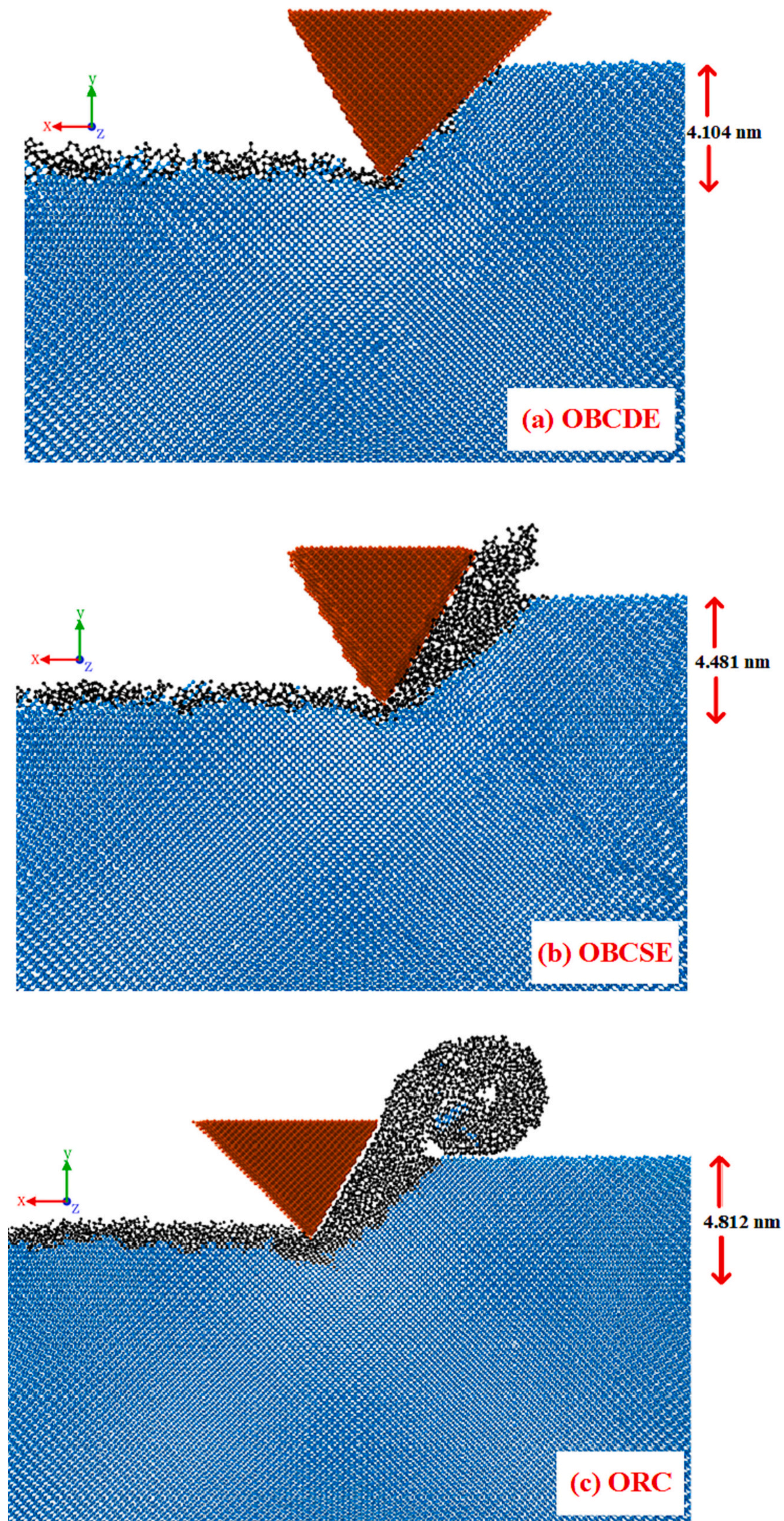

Fig. 12. The morphology of sub-surface plastic deformation of the single crystal GaAs workpiece under three cutting configurations.

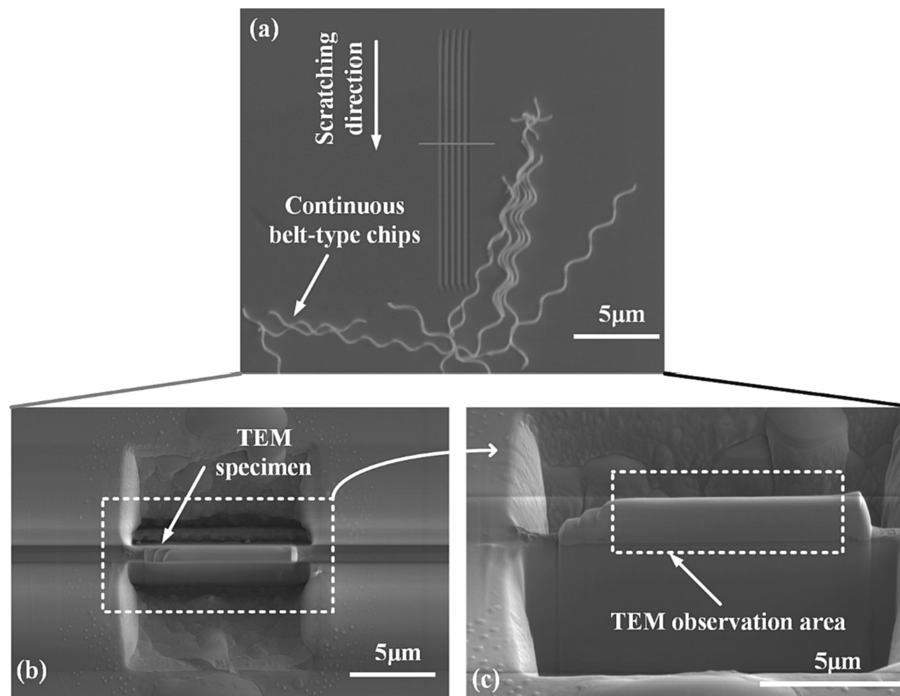

Fig. 13. (a) The morphology of the nanogrooves, (b) The location of the specimen preparation by FIB in situ, (c) The location of TEM observation.

filtered image Fig. 14(d) commensurate with the MD results (see Fig. 14 (e)). From these TEM observations, the *d* spacing was estimated to be about 0.32 nm ($d_{111} = 5.65/\sqrt{3} = 3.26$ Å $= 0.32$ nm) which matches with the lattice parameter calculations of the MD model revealing a nice correlation between the MD and experimental results in terms of the bond length.

In the deformation area, the GaAs lattice was seen to be damaged accompanied by various stacking faults and dislocations shown in Fig. 14(f–g) with their FFT patterns shown in Fig. 14(h). FFT showed a diffuse ring along with the diffraction spots due to the groove surface having an amorphous layer at the uppermost layer. The area normal to the AFM tip was severely damaged resulting in the massive formation of stacking faults and dislocations as shown in Fig. 14(i–j). In addition, at the inset of Fig. 14(i), the FFT pattern did not show a diffuse ring due to the existence of only stacking faults and dislocations in the deeper lattice zones. The d-spacing profile of (111) planes shown in the inset of Fig. 14 (j), was seen to vary from 0.32 nm to 0.28 nm due to dislocations impeding the lattice and a forest of dislocations impeded further damage of the lattice.

Another aspect observed from the TEM investigation was that almost all dislocations extended along the $(\bar{1}\,\bar{1}\,\bar{1})$ and $(\bar{1}\,1\,1)$ planes. This suggests that the {1 1 1} is the slip system in the sub-surface plastic deformation in the processing of single crystal GaAs. However, the dislocation type in the sub-surface plastic deformation layer is not able to be judged in the TEM investigation [42]. To reveal the slip mechanism of the sub-surface plastic deformation of scratched GaAs, the type and distribution of dislocation nucleation were investigated from the MD simulations shown in Fig. 15. It shows the forest of dislocations nucleation with a total of about 10 dislocation segments comprising $1/2\langle110\rangle$ dislocations in the sub-surface of scratched GaAs. Therefore, in light of the dislocation type ($1/2\langle110\rangle$) obtained from the MD simulation results, it can be said that the shuffle-set slip mechanism causes the sub-surface plastic deformation during the nanometric processing of single crystal GaAs [43].

4. Conclusions

In this paper, the influence of tip alignment in AFM-based nanomachining was investigated. Outputs such as the machining quality, depth and propensity of damage to the GaAs substrate after machining, specific cutting energy, coefficient of friction leading to the changes in the mode of material removal and corresponding surface generation process were investigated. The investigative route involved the use of AFM-based nanomachining experiments, TEM inspection and MD simulations. Based on the discussions made, the following broad conclusions can be drawn:

1. The orientation of the cutting tip can change the way the dislocation manifests, nucleate, emit and propagates which changes the mechanisms associated with the transport of plasticity we observe at macroscale while practicing oblique and orthogonal cutting conditions. These early stage avalanches of atomic events influence the macroscopic coefficient of friction besides making implications on the shearing and friction energy between the tool and workpiece. For example, during conventional orthogonal cutting, extra energy is involved in dragging the cut material ahead of the cutting tool and rolling it ahead of the cutting edge. A novel configuration of the oblique cutting with double edge (OBCDE) engagement showed the highest energy efficiency which could preferably be used by the manufacturers while using AFM-based nanomachining.
2. A shuffle-set slip mechanism with {1 1 1} slip system and $1/2\langle1\ 1\ 0\rangle$ type dislocation was found to be responsible for the observed dislocation mediated mass and plasticity transport mechanisms in GaAs both using the MD simulations and the experimental TEM investigations.
3. HRTEM investigations showed amorphization in the top layer in GaAs suggesting this to be the final fate of GaAs after cutting. It also revealed changes in the atomic lattice structure in the vicinity of accumulated stacking faults in the sub-surface of the GaAs.

Fig. 14. (a) The bright field TEM image of GaAs at scratch area; (b) selected area diffraction pattern from image (a); (c) HRTEM image from the groove evolved from scratching; (d) FFT filtered image of image (c); (e) MD simulated scratched GaAs; (f) HRTEM image from the deep groove evolved by scratching of GaAs; (g) FFT filtered image of (f); (h) Fast Fourier Transform of image (f); (i) FFT filtered HRTEM image (inset shows the FFT); (j) FFT filtered image of (i) using selected diffraction spot (red encircled spots). (For interpretation of the references to color in this figure legend, the reader is referred to the web version of this article.)

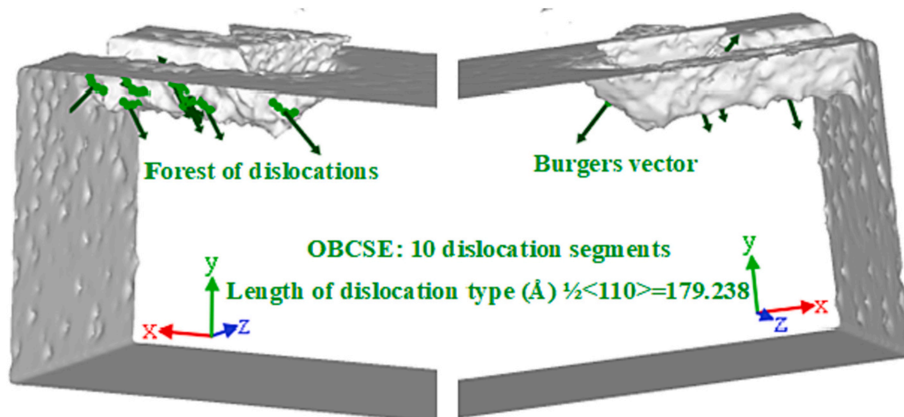

Fig. 15. Distribution of dislocations in the sub-surface of scratched GaAs substrate.

CRediT authorship contribution statement

Pengfei Fan: Conceptualization, Methodology, Investigation, Resources, Data Curation, Writing-original draft
Nirmal Kumar Katiyar: Writing - reviewing and editing, Analysis and illustration
Saurav Goel: Methodology, Formal Analysis, Resources, Supervision, Project administration
Yang He: Resources and Supervision
Yanquan Geng: Experimental support, Resources and Supervision
Yongda Yan: Experimental support, Resources and Supervision
Hui Mao: Experimental support
Xichun Luo: Writing-reviewing, Funding acquisition, editing and Supervision

Declaration of competing interest

The authors declare that they have no known competing financial interests or personal relationships that could have appeared to influence the work reported in this paper.

Acknowledgement

XL gratefully acknowledge the financial support from the EPSRC (EP/K018345/1, EP/T024844/1 and EP/V055208/1), the International Cooperation Program of China (No. 2015DFA70630), Royal Society-NSFC International Exchange scheme (IEC\NSFC\181474) and Science and Technology Based for Equipment Design and Manufacturing for Introduction Talents of Discipline to Universities 2.0 of the 111 project (Project No. BP0719002) for this research.

SG acknowledges the financial support provided by the UKRI via Grants No. EP/S036180/1, EP/T001100/1 and EP/T024607/1, feasibility study awards to LSBU from the UKRI National Interdisciplinary Circular Economy Hub (EP/V029746/1) and Transforming the Foundation Industries: a Network+ (EP/V026402/1), the Hubert Curien Partnership award 2022 from the British Council, Transforming the Partnership award from the Royal Academy of Engineering (TSP1332) and the Newton Fellowship award from the Royal Society (NIF\R1\191571). This work also accessed the Isambard Bristol, UK supercomputing service via Resource Allocation Panel (RAP) as well as ARCHER2 resources (Project e648). The authors also acknowledge the use of the EPSRC (EP/K000586/1) funded ARCHIE-WeSt High-Performance Computer at the University of Strathclyde.

Data statement

All data underpinning this publication are openly available from the University of Strathclyde Knowledge Base.

References

[1] Rao SK, Prasad R. Impact of 5G technologies on industry 4.0. Wirel. Pers. Commun. 2018;100(1):145–59.
[2] Ahn HJ, Il Chang W, Kim SM, Park BJ, Yook JM, Eo YS. 28 GHz GaAs pHEMT MMICs and RF front-end module for 5G communication systems. Microw Opt Technol Lett 2019;61(4):878–82.
[3] Nitesh RS, Rajendran J, Ramiah H, Manaf AAbd. A 700MHz to 2.5GHz cascode GaAs power amplifier for multi-band pico-cell achieving 20dB gain, 40dBm to 45dBm OIP3 and 66% Peak PAE. IEEE Access 2018;6:818–29.
[4] Chu C, Liao X. One to 40 GHz ultra-wideband RF MEMS direct-contact switch based on GaAs MMIC technique. IET Microwaves Antennas Propag 2018;12(6):879–84.
[5] Xie H, Cheng YJ, Fan Y. A K-band high interference-rejection GaAs low-noise amplifier using multizero control method for satellite communication. IEEE Microwave Wireless Compon Lett 2020;30(11):1–4.
[6] Wang S, Pirouz P. Mechanical properties of undoped GaAs. III: indentation experiments. Acta Mater 2007;55(16):5526–37.
[7] Gangopadhyay A, Maros A, Faleev N, Smith DJ. Strain relaxation in low-mismatched GaAs/GaAs 1–x sb x /GaAs heterostructures. Acta Mater 2019;162:103–15.
[8] Zhang W, et al. In-situ laser nano-patterning for ordered InAs/GaAs(001) quantum dot growth. Appl Phys Lett 2018;112(15):1–5.
[9] Hernández-Saz J, Herrera M, Molina SI, Stanley CR, Duguay S. Atom probe tomography analysis of InAlGaAs capped InAs/GaAs stacked quantum dots with variable barrier layer thickness. Acta Mater 2016;103:651–7.
[10] Wu YH, Chang L. Chemical polishing method of GaAs specimens for transmission electron microscopy. Micron 2010;41(1):20–5.
[11] Mcmeekin SG, Robertson M, Mcgheeb L, Winfield JM. Chemimechanical polishing of gallium arsenide to subnanometre surface finish. J Mater Chem 1992;2(3):367–8.
[12] Sasani K, Abbasi SP, Kolian BSabrlouy, Zabihi MS, Sabbaghzadeh J. Relationship between concentration, time and surface roughness of gaas wafer in lapping process: an experimental investigation. In: 2011 symposium on photonics and optoelectronics, SOPO 2011; 2011. p. 1–4.
[13] Prakash SJ, Tyagi R, Gupta A. Backside thinning of GaAs wafer by lapping using DOE approach. In: India international conference on power electronics, IICPE 2010; 2011. p. 1–4.
[14] Ma Y, Ballesteros G, Zajac JM, Sun J, Gerardot BD. Highly directional emission from a quantum emitter embedded in a hemispherical cavity. Opt Lett 2015;40(10):2373.
[15] Chen J, Luo X, Ding F, Rao X, Zhang J. Fundamental study of diamond turning of single crystal gallium arsenide. Precis Eng 2020;62:71–82.
[16] Binnig E, Rohrer G, Gerber H, Weibel C. Surface studies by scanning tunneling microscopy. Phys Rev Lett 1982;49(1):57–61.
[17] Yan Y, Geng Y, Hu Z. Recent advances in AFM tip-based nanomechanical machining. Int J Mach Tool Manuf 2015;99:1–18.
[18] Garcia R, Knoll AW, Riedo E. Advanced scanning probe lithography. Nat Nanotechnol 2014;9(8):577–87.
[19] Fang F, et al. Towards atomic and close-to-atomic scale manufacturing. Int J Extrem Manuf 2019;1(1):012001.
[20] Kaestner M, Hofer M, Rangelow IW. Nanolithography by scanning probes on calixarene molecular glass resist using mix-and-match lithography. J Micro/Nanolithogr MEMS MOEMS 2013;12(3):031111.
[21] Ryu YK, Garcia R. Advanced oxidation scanning probe lithography. Nanotechnology 2017;28(14).
[22] Fan P, et al. Scanning probe lithography: state-of-the-art and future perspectives. Micromachines 2022;13(2).
[23] Wang S, Pirouz P. Mechanical properties of undoped GaAs. II: the brittle-to-ductile transition temperature. Acta Mater 2007;55(16):5515–25.
[24] Chavoshi SZ, Xu S, Goel S. Addressing the discrepancy of finding the equilibrium melting point of silicon using molecular dynamics simulations. Proc R Soc A Math Phys Eng Sci 2017;473(2202):1–9.
[25] Popov VV. Powder bed fusion additive manufacturing using critical raw materials: a review. Materials 2021;14(4).
[26] Pan Y. New insights into the methods for predicting ground surface roughness in the age of digitalisation. Precis Eng 2021;67(October 2020):393–418.
[27] Hyon CK, Choi SC, Hwang SW, Ahn D, Kim Y, Kim EK. Direct nanometer-scale patterning by the cantilever oscillation of an atomic force microscope. Appl Phys Lett 1999;75(2):292–4.
[28] Fang TH, Chang WY, Huang JJ. Dynamic characteristics of nanoindentation using atomistic simulation. Acta Mater 2009;57(11):3341–8.
[29] Goel S, et al. Horizons of modern molecular dynamics simulation in digitalized solid freeform fabrication with advanced materials. Mater Today Chem 2020;18:100356.
[30] Goel S, Kovalchenko A, Stukowski A, Cross G. Influence of microstructure on the cutting behaviour of silicon. Acta Mater 2016;105:464–78.
[31] Fan P, Goel S, Luo X, Upadhyaya HM. Atomic - scale friction studies on single - crystal gallium arsenide using atomic force microscope and molecular dynamics simulation. Nanomanufacturing Metrol 2021;(0123456789).
[32] Goel S, Martinez FD, Chavoshi SZ, Khatri N, Giusca C. Molecular dynamics simulation of the elliptical vibration-assisted machining of pure iron. J Micromanufacturing 2018;1(1):6–19.
[33] Khatri N, Barkachary BM, Muneeswaran B, Al-Sayegh R, Luo X, Goel S. Surface defects incorporated diamond machining of silicon. Int J Extrem Manuf 2020;2(4):45102.
[34] Plimpton SJ. Fast parallel algorithms for short range molecular dynamics. J Comput Phys 1995;117:1–19.
[35] Stukowski A. Visualization and analysis of atomistic simulation data with OVITO-the open visualization tool. Model Simul Mater Sci Eng 2010;18(1). pp.
[36] Murdick DA, Zhou XW, Wadley HNG, Nguyen-Manh D, Drautz R, Pettifor DG. Analytic bond-order potential for the gallium arsenide system. Phys Rev B Condens Matter Mater Phys 2006;73(4):1–20.

[37] Ward DK, Zhou XW, Wong BM, Doty FP, Zimmerman JA. Analytical bond-order potential for the cadmium telluride binary system. Phys Rev B Condens Matter Mater Phys 2012;85(11):1–19.
[38] Ziegler JF, Ziegler MD, Biersack JP. SRIM - the stopping and range of ions in matter (2010). Nucl Instruments Methods Phys Res Sect B Beam Interact with Mater Atoms 2010;268(11–12):1818–23.
[39] Goodwin L, Goringe CM, Bowler DR, Sutton AP, Finnis MW. Generating transferable tight-binding parameters: application to silicon. Europhys Lett 1989;9 (7):701–6.
[40] Merchant ME. An interpretive look at 20TH century research on modeling of machining. Mach Sci Technol Dec. 1998;2(2):157–63.
[41] Wang B, Liu Z, Song Q, Wan Y, Shi Z. Proper selection of cutting parameters and cutting tool angle to lower the specific cutting energy during high speed machining of 7050–T7451 aluminum alloy. J Clean Prod 2016;129:292–304.
[42] Wu Z, Liu W, Zhang L, Lim S. Amorphization and dislocation evolution mechanisms of single crystalline 6H-SiC. Acta Mater 2020;182:60–7.
[43] Ganchenkova M, Nieminen RM. Mechanical properties of silicon microstructures. Elsevier Inc.; 2015.